JACS Au
AN OPEN ACCESS JOURNAL OF THE AMERICAN CHEMICAL SOCIETY

pubs.acs.org/jacsau

Article

Hybrid Carbon Dot Assembly as a Reactive Oxygen Species Nanogenerator for Ultrasound-Assisted Tumor Ablation

Deblin Jana, Dongdong Wang, Praveenbalaji Rajendran, Anivind Kaur Bindra, Yi Guo, Jiawei Liu, Manojit Pramanik, and Yanli Zhao*

Cite This: *JACS Au* 2021, 1, 2328–2338

Read Online

ACCESS | Metrics & More | Article Recommendations | Supporting Information

ABSTRACT: The efficacy of reactive oxygen species (ROS)-based therapy is substantially constrained by the limited ROS generation, stern activation conditions, and lack of a straightforward reaction paradigm. Carbon dots (CDs) have been highly sought after for therapeutic applications for their biocompatibility and intrinsic fluorescence imaging capabilities, making them suitable for ROS generation. Herein, we synthesized a CD-based ultrasmall hybrid nanostructure possessing active sites of Mo, Cu, and IR-780 dye. After cooperative self-assembly with 1,2-distearoyl-*sn*-glycero-3-phosphoethanolamine-poly(ethylene glycol), the obtained assembly (CMIR-CDa) exhibits near-infrared fluorescence imaging and photoacoustic tomography. Interestingly, CMIR-CDa can generate singlet oxygen ($^1O_2$), hydroxyl radical (·OH), and superoxide radical anion ($O_2^{\bullet -}$) upon ultrasound stimulus owing to its sonosensitizing and enzyme-mimicking properties, showing an enhanced efficacy for tumor ablation *in vivo*. The collective *in vitro* and *in vivo* results indicate that CMIR-CDa has a high potency as an ROS nanogenerator under US irradiation, even at a low concentration. The present study offers an approach for engineering hybrid CDs in a bioinspired way for intratumoral ROS augmentation in response to deep tissue penetrable external stimuli.

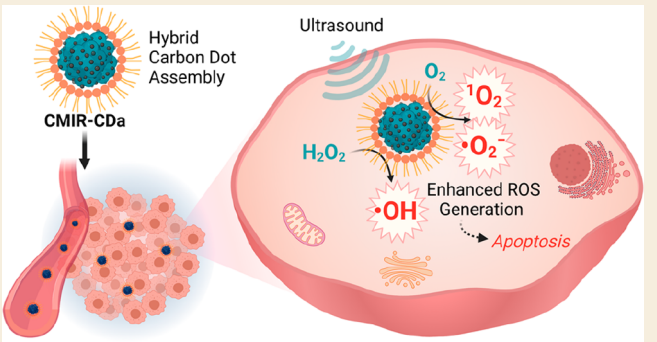

KEYWORDS: *chemodynamic therapy, hybrid nanostructure, reactive oxygen species, sonodynamic therapy, ultrasound*

INTRODUCTION

Reactive oxygen species (ROS) that mostly consist of singlet oxygen ($^1O_2$), hydroxyl radical (·OH), and superoxide radical anion ($O_2^{\bullet -}$) operate as regulatory essentials at the cellular level.[1,2] However, the concentration raise of ROS to an anomalous level or a deficiency of active antioxidants can cause a significant damage to cells.[3,4] A tumor microenvironment (TME) adopts an equilibrium state encompassing both elevated ROS levels and high antioxidant mechanisms. Thereby, cancer cells, having a lower oxidative stress threshold, are more susceptible to ROS-mediated damage.[5] To disrupt cellular self-adapting mechanisms, both photodynamic therapy (PDT) and chemodynamic therapy (CDT), have shown significant applicability in cellular ROS generation. Briefly, type I PDT can generate multiple cytotoxic species, e.g., hydrogen peroxide (H_2O_2), ·OH, and $O_2^{\bullet -}$, by electron transfer from an excited photosensitizer to O_2 and other organic molecules, whereas type II PDT produces cytotoxic $^1O_2$ from O_2.[3] Bacteriochlorin incorporated nanosystems are often utilized for both type I and type II PDT upon laser irradiation, showing considerable tolerance to the hypoxia.[6−8] However, bacteriochlorin is mostly unstable toward light and O_2, hindering its potency for practical purposes. On the one hand, CDT utilizes Fenton or Fenton-like catalysts to transform overexpressed H_2O_2 in TME (from 100 μM to 1 mM) into cytotoxic ·OH.[9,10] The synergism between type II PDT and CDT has been examined because of a better therapeutic outcome through multiple ROS generation.[11−14] On the other hand, nanosystems consisting of both type I and type II PDT capacities were explored recently.[6,15] Although such nanosystems show commendable tumor ablation *in vivo*, practical applications are often hindered by complicated synthetic pathways and uses of UV or visible light source as the external stimuli.[16] Thus, multiple ROS nanogenerators with a straightforward synthetic paradigm have been highly sought after in the best interest of enhanced theranostics.

Carbon dots (CDs) have received considerable attention for their unique characteristics like low synthetic cost, good biocompatibility, high photostability, competent catalytic

Received: September 24, 2021
Published: November 13, 2021

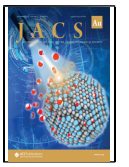

https://doi.org/10.1021/jacsau.1c00422
JACS Au 2021, 1, 2328−2338

Scheme 1. Schematic Diagram for the Synthesis of CMIR-CDa[a]

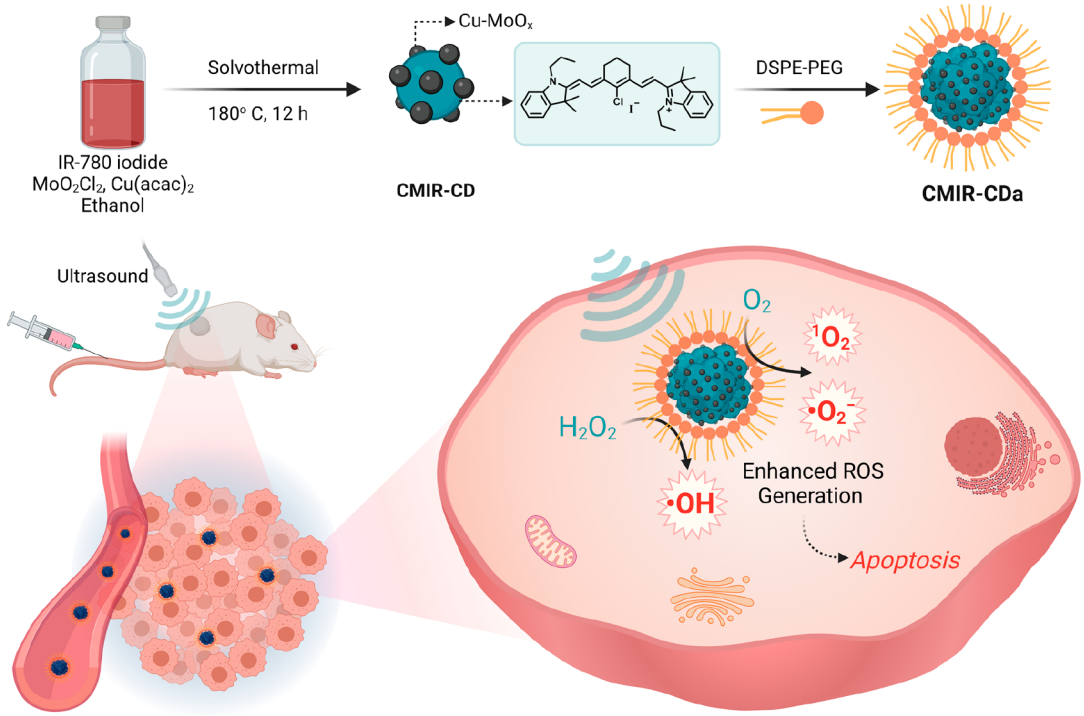

[a]CMIR-CDa exhibits enhanced cytotoxic ROS generation in the presence of US irradiation in a tumor microenvironment. Created with Biorender.com under a granted license.

efficiency, and flexible surface functionality.[17−19] Despite being limited by an inflexible synthesis methodology to generate $^1O_2$ intrinsically, CDs have been utilized as nanoscale photosensitizers. A current methodology includes using commercially available photosensitizers as the precursor in the synthetic paradigm to incorporate photodynamic properties in CDs.[20,21] As a replacement for PDT, sonodynamic therapy (SDT) utilizes the nonthermal effect of ultrasound (US) in combination with a sonosensitizer.[22] The US being precisely focused at the tumor site and possessing a penetration ability to deeply seated human soft tissues is often advantageous over traditional light-induced therapeutic pathways.[23,24] The sonosensitizers can absorb the low-density US energy applied, followed by the release of the received energy when they return to the ground state from the excited state. The O_2 molecule interacts with the released energy and transforms to $^1O_2$, which then initiates a sequence of oxidization reactions and eventually leads to the tumor cell ablation.[25,26] Recently, IR-780 iodide was reported to be a class of organic sonosensitizer to treat breast cancer.[27] IR-780, having a peak optical absorption at around 780 nm, has appeared as a promising fluorescent probe for tumor fluorescence imaging owing to the high fluorescence intensity and physiological stability.[28−30] Thus, utilizing IR-780 as the precursor in the CD formation can generate a type of CDs for SDT of cancer, while maintaining the fluorescence properties for fluorescence imaging.

However, IR-780 derived CDs may predominantly generate $^1O_2$ through SDT, which would hinder the goal of achieving a multiple ROS nanogenerator. Hybridization of such CDs by incorporating metal ions acting as Fenton or Fenton-like catalysts for ROS generation can lead to a feasible solution. Copper ions (Cu^+/Cu^{2+}) were proposed to undergo a Fenton-like reaction in weakly acidic and neutral conditions with about 160-fold enhancement of reaction rate compared to that widely used iron redox couple ($Fe^{2+/3+}$).[31−33] Additionally, the coupling of copper (Cu^+/Cu^{2+}) and molybdenum (Mo^{4+}/Mo^{6+}) was studied to exhibit excellent ·OH generation ability *via* Fenton-like reaction for CDT.[34−36] The presence of Mo^{5+}/Mo^{6+} on a nanoparticle surface was reported to promote the formation of cytotoxic $O_2^{\bullet-}$ from O_2 in acidic TME by a couple of tandem reactions.[37] Recently, a hollow Cu_2MoS_4 nanostructure was reported to produce $O_2^{\bullet-}$ in the presence of 1064 nm light apart from PTT and CDT.[38] Therefore, the introduction of Cu and Mo on the skeleton of IR-780 decorated CDs would lead to the formation of a multiple ROS generator, which could be activated by both internal and external stimuli, i.e., TME and US, respectively.[39]

Herein, we report fluorescent hybrid CDs, namely, CMIR-CDa, synthesized from a mixture of copper(II) acetylacetonate ($Cu(acac)_2$), molybdenum dichloride dioxide (MoO_2Cl_2), and IR-780 iodide, followed by cooperative self-assembly with 1,2-distearoyl-sn-glycero-3-phosphoethanolamine-poly(ethylene glycol) (DSPE-PEG) to increase the biocompatibility and aqueous dispersity (Scheme 1). The as-prepared hybrid CDs exhibited near-infrared (NIR) emission, high physiological stability, and efficient generation of $^1O_2$ and $O_2^{\bullet-}$ under US irradiation. The elevated H_2O_2 level in TME is responsible for the interaction with Cu^+/Cu^{2+} and Mo^{4+}/Mo^{6+} redox couple to generate cytotoxic ·OH *via* Fenton-like reactions. The application of US generates strong shock waves to produce cavitation bubbles with intensive local turbulence, and thus, the mass transfer rate is augmented in homogeneous and heterogeneous systems of Fenton reagents. Thereby, the CDT performance of CMIR-CDa was augmented in the presence of US irradiation.[40] This smart CMIR-CDa nanosystem acting as

https://doi.org/10.1021/jacsau.1c00422
JACS Au 2021, 1, 2328−2338

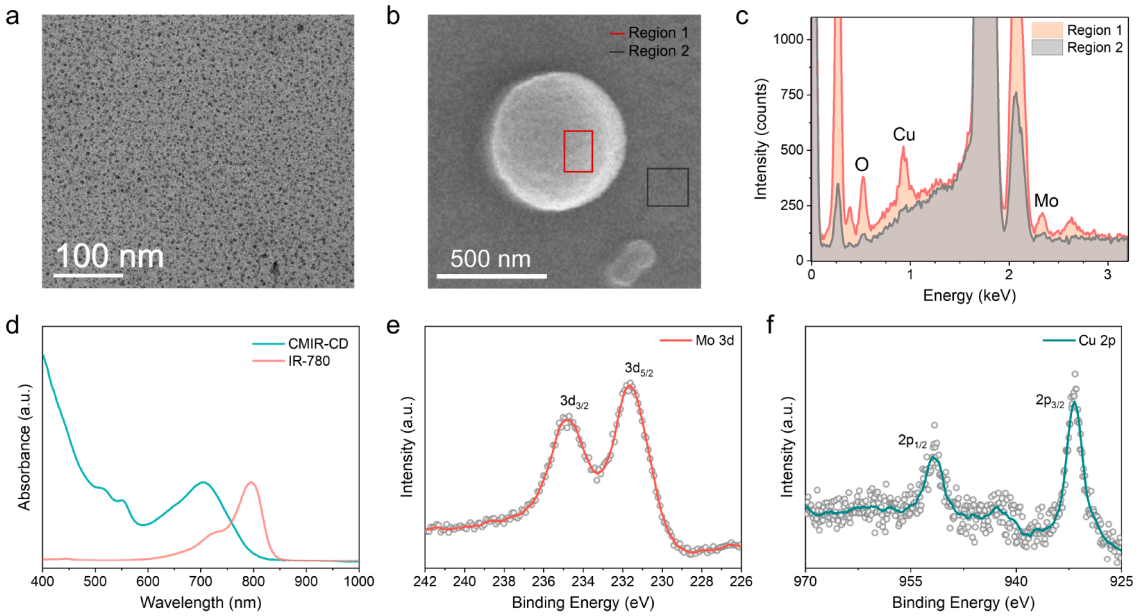

Figure 1. (a) TEM image of CMIR-CD. (b) SEM image of assembled CMIR-CD. (c) Corresponding SEM EDS of CMIR-CD. (d) UV−vis−NIR absorption spectra of CMIR-CD and IR-780 iodide in ethanol. (e) High-resolution X-ray photoelectron spectroscopy (XPS) of Mo 3d for CMIR-CD. (f) High-resolution XPS of Cu 2p for CMIR-CD.

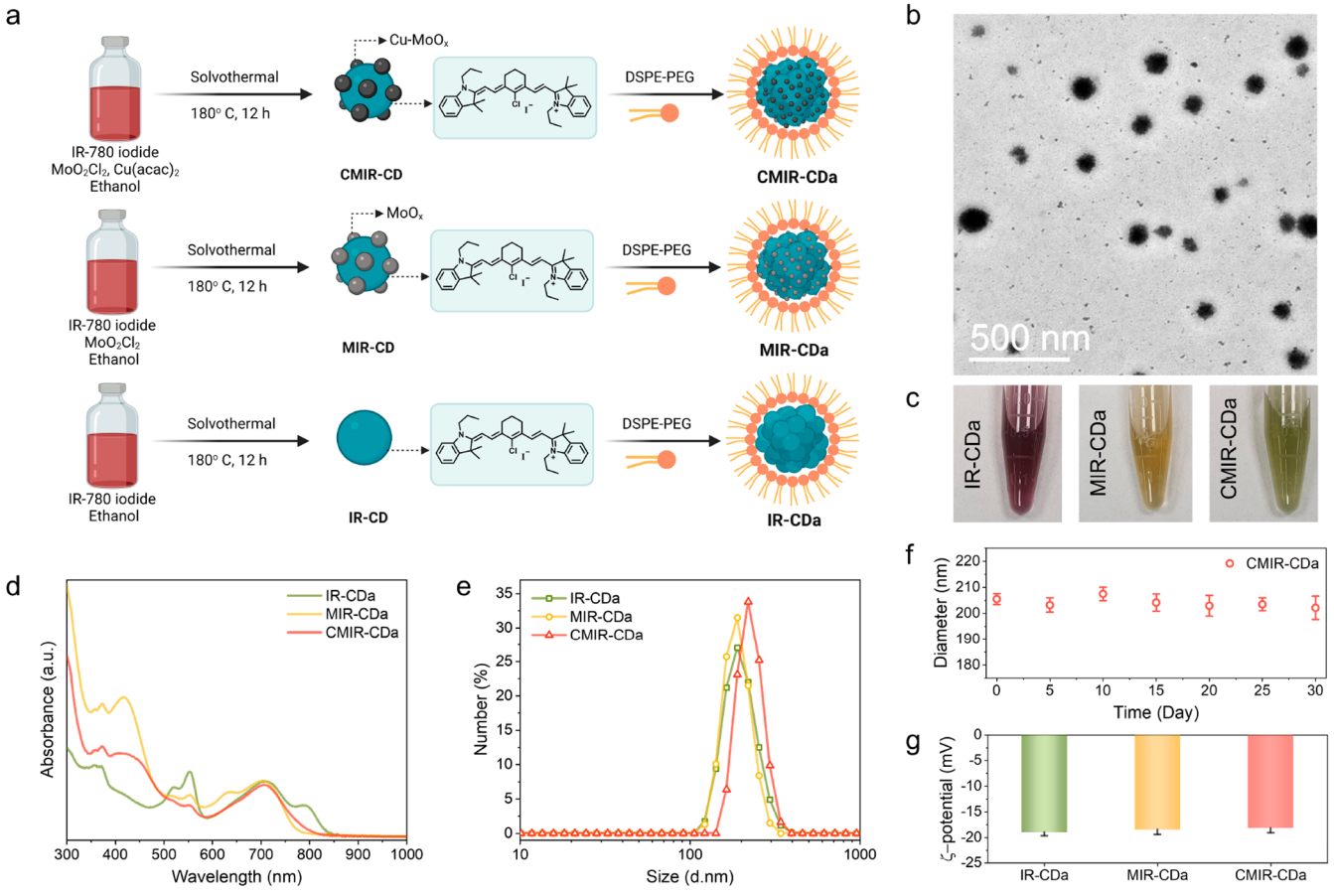

Figure 2. (a) Schematic illustration for the preparation of IR-CDa, MIR-CDa, and CMIR-CDa. Created with Biorender.com under a granted license. (b) TEM image of CMIR-CDa. (c) Photos of PBS solutions containing IR-CDa, MIR-CDa, and CMIR-CDa. (d) UV−vis−NIR absorption spectra of IR-CDa, MIR-CDa, and CMIR-CDa. (e) Dynamic light scattering (DLS) analysis of IR-CDa, MIR-CDa, and CMIR-CDa. (f) Long-term aqueous stability of CMIR-CDa determined by DLS over 30 days (n = 3). (g) ζ potentials of IR-CDa, MIR-CDa, and CMIR-CDa (n = 3).

https://doi.org/10.1021/jacsau.1c00422
JACS Au 2021, 1, 2328−2338

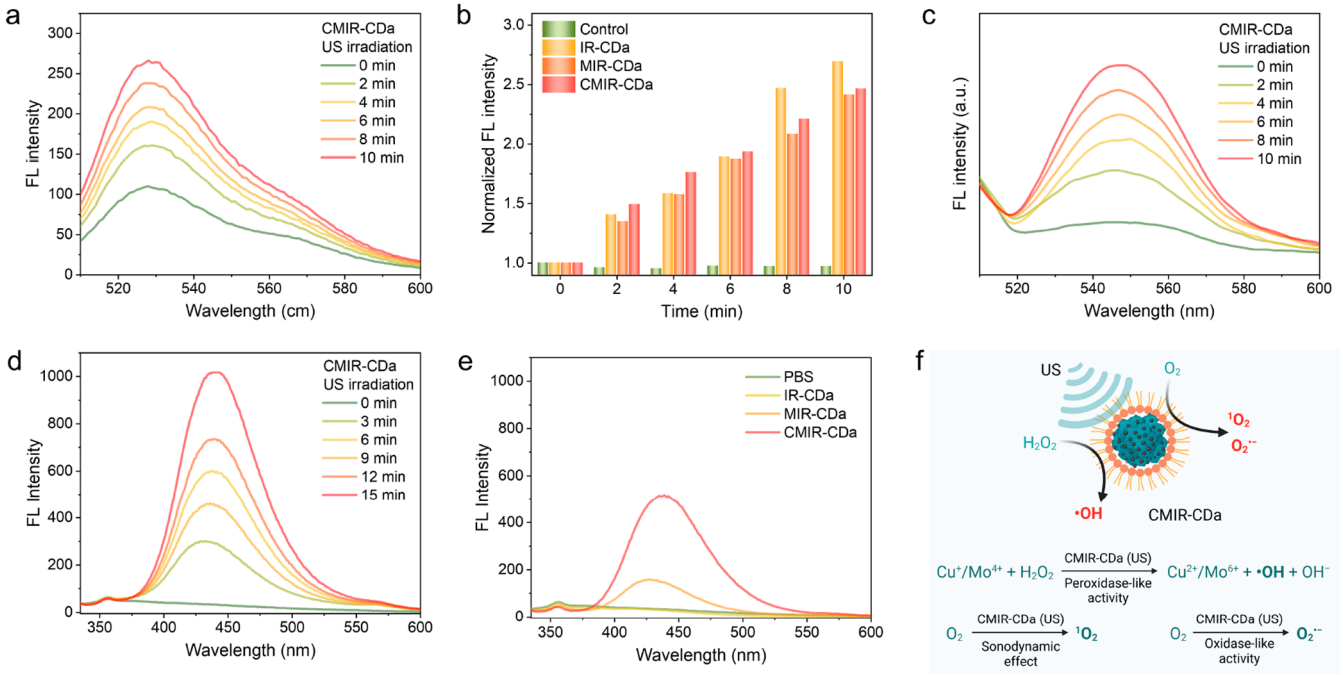

Figure 3. (a) Singlet oxygen sensor green (SOSG) assay for $^1O_2$ generation ability of CMIR-CDa under US irradiation (0.5 W cm^{-2}). (b) Comparison of $^1O_2$ generation ability by different groups under US irradiation. (c) DHR 123 assay for $O_2^{\bullet -}$ generation ability of CMIR-CDa under US irradiation (0.5 W cm^{-2}). (d) Terephthalic assay for ·OH generation ability of CMIR-CDa under US irradiation (0.5 W cm^{-2}). (e) Comparison of ·OH generation ability by different groups under US irradiation. (f) Schematic representation of ROS generation ability by CMIR-CDa under US stimuli. Created with Biorender.com under a granted license. FL: Fluorescence.

a multiple ROS ($^1O_2$, ·OH, and $O_2^{\bullet -}$) generator and a fluorescence and photoacoustic tomography agent presents a commendable tumor inhibition effect *in vivo* (Scheme 1).

RESULTS AND DISCUSSION

Synthesis and Characterization of CMIR-CDa

The CDs (CMIR-CD) were synthesized by following a solvothermal approach from $Cu(acac)_2$, MoO_2Cl_2, and IR-780 iodide with absolute ethanol as the solvent. The solution was heated at 180 °C for 12 h to obtain ultrasmall CMIR-CD soluble in ethanol. The transmission electron microscopy (TEM) image of CMIR-CD showed a uniform distribution of CDs with an average diameter of ≈5 nm (Figure 1a). Elemental distribution of the Mo, Cu, and O elements in CMIR-CD was assessed by scanning electron microscopy energy-dispersive X-ray spectroscopy (SEM EDS, Figure 1b,c). For the SEM EDS sample preparation, the hydrophobic CMIR-CD was aggregated by the dialysis against water. The elements are distributed throughout the surface of the CD backbone as their oxide forms. As the main precursor IR-780 iodide and CMIR-CD are both hydrophobic, the absorption and emission spectra were recorded by solubilizing the same in ethanol. The absorption peak blue-shifted to 704 nm for CMIR-CD compared to 790 nm for free IR-780 iodide (Figure 1d). Corresponding to the absorption spectra, the emission spectra of CMIR-CD blue-shifted as well compared to those of free IR-780 iodide (Figure S1). The blue shift of maximum emission could be attributed to the *J*-aggregation of IR-780 iodide formed during the synthesis process of the hybrid CDs.

Fourier transform infrared (FT-IR) spectra indicated that CMIR-CD holds the characteristic peaks of IR-780 iodide, suggesting a successful synthetic route (Figure S2). To determine the presence of multiple elements, the X-ray photoelectron spectroscopy (XPS) spectrum of CMIR-CD was measured (Figure 1e,f and Figure S3). The high-resolution XPS spectrum showed the presence of individual elements, namely, Mo, Cu, C, and O. Due to high-temperature solvothermal synthetic pathway with an oxidative environment, the obtained CMIR-CD exhibited metallic-oxide-like properties. XPS results revealed that Mo (3d) was mainly in a mixture of different oxidation states, with a strong resemblance to MoO_x-like nanostructures. The positions of the Cu (2p) XPS peaks and the satellite peaks indicated the presence of (Cu^{2+}/Cu^{+}) oxidation states. It can be inferred that, in the synthetic process, IR-780 tends to form the CD core decorated with nanostructured oxides of Mo and Cu to form the final hybrid CD structure.

To address the water solubility issue of CMIR-CD, DSPE-PEG was utilized to induce cooperative self-assembly with CMIR-CD owing to the hydrophobic−hydrophobic interactions in an aqueous solution (Figure 2a). The assembled nanoparticles, designated as CMIR-CDa, possessed high physiological stability in water and phosphate-buffered saline (PBS). The TEM images indicated that CMIR-CDa possessed a spherical nanostructure with an average diameter of ≈200 nm (Figure 2b). To investigate the properties of individual components in CDs, two control systems (IR-CDa and MIR-CDa) were synthesized. IR-CDa was synthesized following similar conditions as that of CMIR-CDa, with IR-780 iodide as the only precursor. MIR-CDa was synthesized by a solvothermal approach from IR-780 iodide and MoO_2Cl_2 using absolute ethanol as the solvent, followed by the assembly with DSPE-PEG. The TEM images of IR-CDa and MIR-CDa showed spherical nanostructures (Figure S4). These nanoparticles were highly stable and dispersible in PBS, terming them suitable for *in vitro* studies (Figure 2c).

https://doi.org/10.1021/jacsau.1c00422
JACS Au 2021, 1, 2328−2338

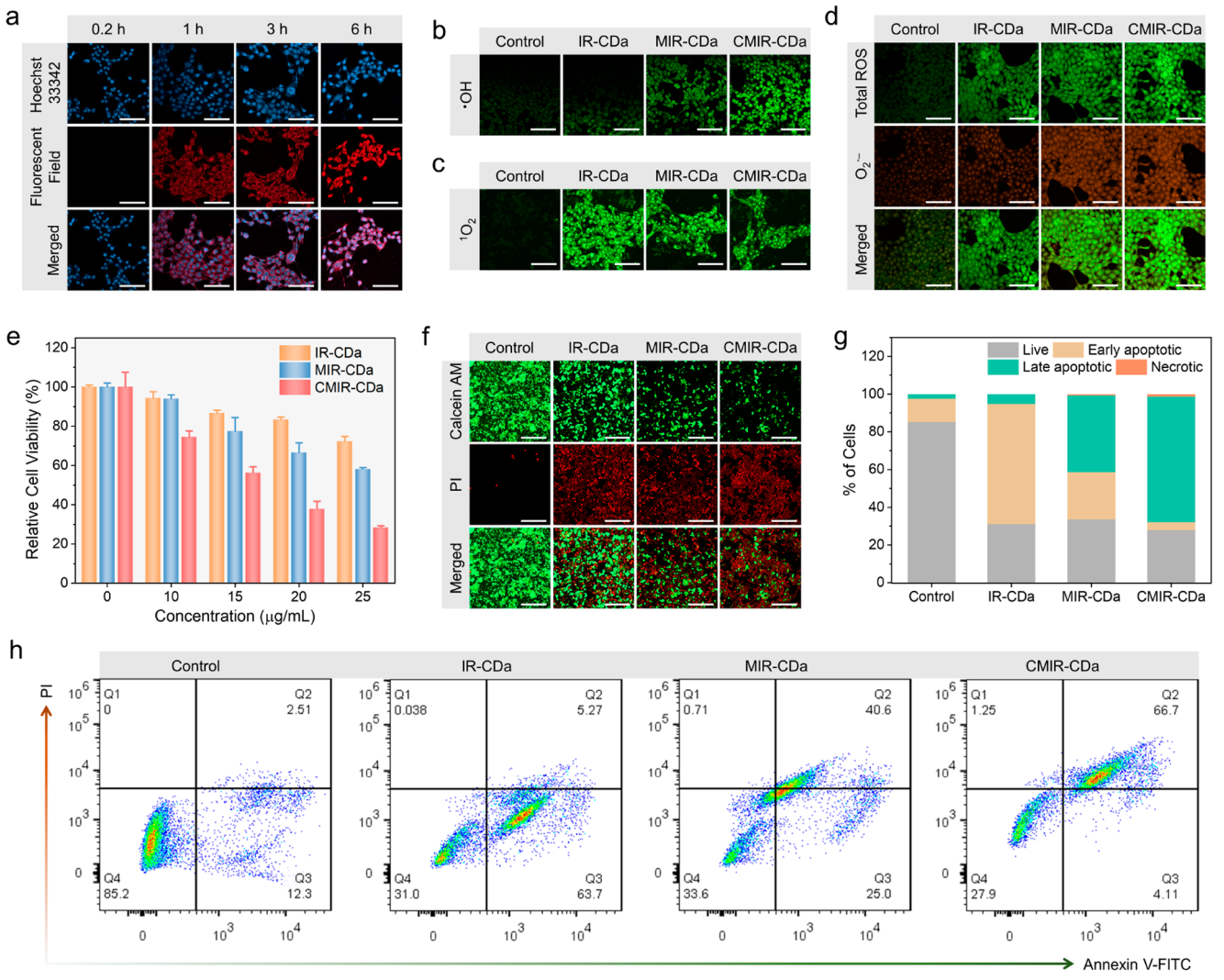

Figure 4. (a) Time-dependent confocal fluorescence imaging of 4T1 cells upon incubation with CMIR-CDa. Scale bar: 100 μm. (b) Confocal images of singlet oxygen sensor green (SOSG) in 4T1 cells by HPF assay with as-indicated treatments upon US application (0.5 W cm^{-2}, 3 min). Scale bar: 100 μm. (c) Confocal images of $^1O_2$ in 4T1 cells by SOSG assay with as-indicated treatments upon US application (0.5 W cm^{-2}, 3 min). Scale bar is 100 μm. (d) Total ROS and $O_2^{\bullet-}$ generation evaluated by superoxide detection assay in 4T1 cells treated by IR-CDa, MIR-CDa, and CMIR-CDa with US irradiation (0.5 W cm^{-2}, 3 min). Scale bar: 100 μm. (e) Cell viability assay of 4T1 cells after different treatments under the US irradiation (1 W cm^{-2}, 3 min, n = 5). (f) Live/dead double staining of 4T1 cells after different treatments under US indicated by calcein-AM (green, live cells) and PI (red, dead cells). Scale bar: 200 μm. (g) Cell populations acquired from flow cytometry apoptosis analysis. (h) Flow cytometry analysis of 4T1 cells after different treatments under US, stained with annexin V-FITC/PI.

CMIR-CDa owned similar absorption spectra and absorption maximum position with CMIR-CD, depicting a successful assembly process. UV−vis spectra of CMIR-CDa, MIR-CDa, and IR-CDa revealed a similar characteristic peak at ∼705 nm (Figure 2d). The emission maximum of CMIR-CDa also possessed a similar position as that of CMIR-CD (Figure S5). The normalized emission spectra presented the emission peaks in the far-red region, promising an effective application in fluorescence imaging. FT-IR spectra showed characteristic peaks for DSPE-PEG after the phase transfer formations of CMIR-CDa, MIR-CDa, and IR-CDa, supporting a successful self-assembly process (Figure S6). Additional studies using dynamic light scattering (DLS) revealed that CMIR-CDa had a hydrodynamic diameter of ≈220 nm, in accordance with the TEM images (Figure 2e). Hydrodynamic diameters of ≈190 and 191 nm were recorded for MIR-CDa and IR-CDa through DLS measurements, respectively. Upon increasing the ratio between DSPE-PEG and CMIR-CD in the preparation process, the size of the self-assembled nanoparticles decreased (Figure S7). CMIR-CD tends to accumulate in the hydrophobic core of the hydrophobicity−hydrophilicity-driven self-assembled nanostructures during the assembly process, thereby gradually increasing the size of the nanoparticles with incremental CMIR-CD amount. The stability of CMIR-CDa aqueous solution was examined through time-dependent DLS analysis, indicating no noticeable aggregation over 30 days (Figure 2f). The ζ potential of ∼ −19 mV was documented for all the groups (Figure 2g), implying that the CD assemblies were suitable to be used for the accumulation in the tumor region through the enhanced permeability and retention effect (EPR) effect.

https://doi.org/10.1021/jacsau.1c00422
JACS Au 2021, 1, 2328−2338

ROS Generation Properties

$^1O_2$ generation in the presence of US irradiation was the foremost motivation behind utilizing IR-780 as the CD precursor. We investigated the production of $^1O_2$ by a singlet oxygen sensor green (SOSG) probe in the presence of CMIR-CDa, MIR-CDa, or IR-CDa in a buffer solution of pH 6.5. The probe exhibits a fluorescence emission enhancement at 525 nm when reacted with $^1O_2$. The generation of $^1O_2$ was amplified when CMIR-CDa was exposed to US irradiation (Figure 3a). In comparison, both MIR-CDa and IR-CDa displayed an enhancement in fluorescence, attributed to the presence of IR-780 in the CD structure (Figure 3b and Figure S8). In addition, CMIR-CDa could only enhance the probe fluorescence under US irradiation in a deoxygenated solution, further confirming an O_2-dependent sonodynamic reaction pathway (Figure S9). MoO_x-based nanostructures were reported to possess an oxidase-mimicking property by generating $O_2^{\bullet -}$ in the presence of external stimuli. We then studied the production of $O_2^{\bullet -}$ by a dihydrorhodamine 123 (DHR 123) probe in the presence of different groups. As expected, CMIR-CDa and MIR-CDa both exhibited fluorescence intensification under the application of US, confirming the generation of $O_2^{\bullet -}$ (Figure 3c). Control group IR-CDa showed a limited fluorescence enhancement when exposed to US, further confirming the importance of MoO_x-based nanoislands on the CD backbone for ROS enhancement (Figure S10).

Next, the production of ·OH through the Fenton or Fenton-like reaction using terephthalic acid (TA) as a probe was investigated. The probe displays a fluorescence emission enhancement at 435 nm upon the reaction to ·OH. With increased US application time, as-produced 2-hydroxy TA exhibited a gradual amplification of fluorescence intensity in the presence of CMIR-CDa (Figure 3d), indicating that the aptitude of the Fenton or Fenton-like reaction could be amplified by the US application. A similar observation was recorded for MIR-CDa upon US application, although a significantly lower concentration of ·OH was generated in comparison to that of CMIR-CDa (Figure S11a). The application of US conveys intense shock waves for producing cavitation bubbles, followed by intense local turbulence, and thus, the rate of mass transfer is enhanced in homogeneous and heterogeneous systems of Fenton reagents. Coupling of Mo^{4+} with Cu^+ would favor the redox potential toward an enhanced Fenton-like reaction, which is further augmented by the introduction of vibrational energy from US. Upon US irradiation, CMIR-CDa produced a higher concentration of singlet oxygen sensor green (SOSG), in comparison to the same conditions deployed without US (Figure S11b). The singlet oxygen sensor green (SOSG) generation ability of CMIR-CDa also decreased upon decreasing the H_2O_2 concentration, further proving the essentiality of H_2O_2 in the Fenton-like reaction (Figure S12). Additionally, IR-CDa and PBS displayed no detectable change in fluorescence under the same conditions, confirming the utility of Fenton agents in the production of singlet oxygen sensor green (SOSG) (Figure 3e). The peroxidase-mimicking activity of CMIR-CDa could couple with the sonodynamic and oxidase-mimicking properties to realize enhanced ROS, exhibiting a high potential in the application of tumor therapy (Figure 3f).[41]

In Vitro Therapy

To investigate the accumulation of the CD assembly in tumor cells, 4T1 cells were cultured and incubated with CMIR-CDa, and fluorescence imaging was then performed. The cytoplasm of the 4T1 cells displayed prominent fluorescence signals in the red channel, leaving the nucleus with blue fluorescence through Hoechst 33342 staining (Figure S13). This observation indicated that CMIR-CDa was internalized into the cells with specific localization in the cytoplasm. Control experiments with MIR-CDa and IR-CDa also displayed similar results, showing that CD composition variation did not have a visible effect on the cellular uptake mechanism. A time-dependent study on the cellular uptake of CMIR-CDa revealed an intensification in fluorescence signals over time, implying a gradual uptake mechanism (Figure 4a).

In order to confirm the ·OH generation capability in 4T1 cells, intracellular ·OH was assessed using a hydroxyphenyl fluorescein (HPF) assay (Figure 4b). Upon exposure to ·OH, nonfluorescent HPF is reacted to show green fluorescence, which can be detected by confocal laser scanning microscopy (CLSM). As expected, CMIR-CDa could produce high concentrations of ·OH upon US irradiation owing to Fenton-like reaction by the redox couple (Cu^+/Mo^{4+}) in the presence of intratumoral H_2O_2, as indicated by the enhancement of green fluorescence. The control studies utilizing MIR-CDa indicated a faint increment in fluorescence upon US application, whereas other control groups were unable to produce substantial ·OH under US to be detected by CLSM. A similar observation was noted when coumarin-3-carboxylic acid assay was used for ·OH detection, indicating enhanced blue fluorescence for CMIR-CDa treated cells (Figure S14). In addition, the intracellular $^1O_2$ generation ability of CMIR-CDa was studied with the SOSG probe, where the probe reacts with $^1O_2$ to produce an endoperoxide product with green fluorescence. 4T1 cells were incubated with CMIR-CDa, MIR-CDa, and IR-CDa for 6 h and subsequently cultured with SOSG for 30 min, respectively. The cells were further irradiated with US and immediately imaged. Green fluorescence was detected in the 4T1 cells for all three groups in disparity to the control PBS group (Figure 4c). However, IR-CDa incubated cells exhibited a stronger fluorescence compared to CMIR-CDa and MIR-CDa, suggesting that the metal oxides in CMIR-CDa and MIR-CDa could promote a minute quenching of $^1O_2$ upon incubation.

We further investigated the superoxide generation capability of CMIR-CDa, as Mo-based oxide nanostructures could often promote $O_2^{\bullet -}$ generation in TME conditions or through external stimuli. A ROS/superoxide detection assay kit was used to determine the concentrations of $O_2^{\bullet -}$ and total ROS produced after US irradiation in 4T1 cells after incubation with CMIR-CDa, MIR-CDa, and IR-CDa, respectively (Figure 4d). Both CMIR-CDa and MIR-CDa produced a substantial amount of $O_2^{\bullet -}$ in comparison to IR-CDa and PBS groups, as indicated by orange fluorescence. The absence of metal oxide moieties in the IR-CDa nanostructure would contribute to its minimal $O_2^{\bullet -}$ generation. Moreover, all the study groups produced a significant amount of green fluorescence in total ROS assay upon US irradiation in contrast to the PBS group. The CMIR-CDa group showed an intensified green fluorescence as compared to the control groups owing to the enhanced ROS generation upon US application (Figure S15).

https://doi.org/10.1021/jacsau.1c00422
JACS Au 2021, 1, 2328−2338

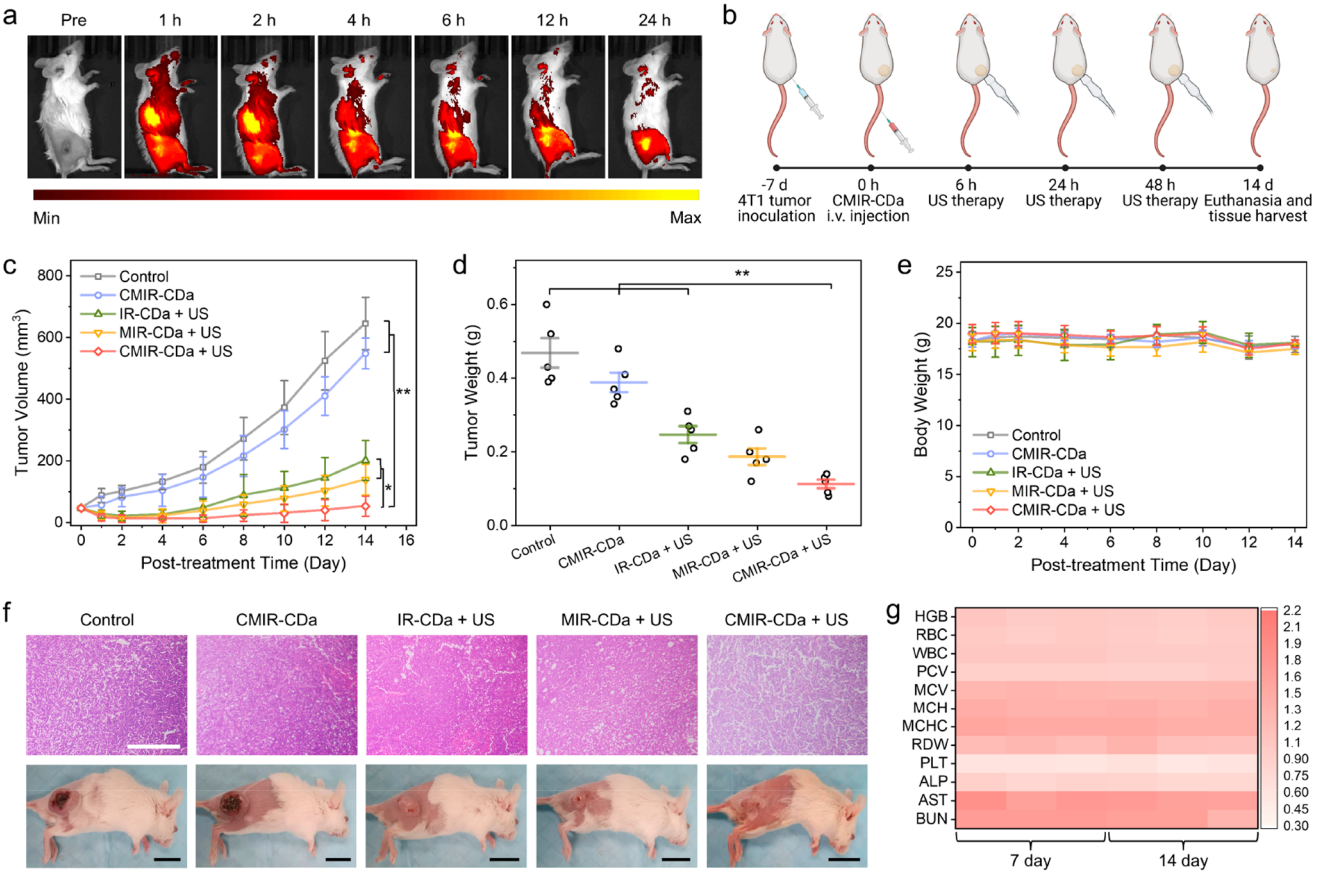

Figure 5. (a) NIR fluorescence imaging of 4T1-tumor-bearing BALB/c mice at different time points after the intravenous injection of CMIR-CDa. (b) Schematic illustration of the *in vivo* treatment schedule. Created with Biorender.com under a granted license. (c) Growth curves of tumors in living mice after various treatments (n = 5). (d) Average weights of tumors harvested from as-indicated treatment groups (n = 5). (e) Average mouse weights from as-indicated treatment groups (n = 5). (f) H&E-stained images of tumor tissues acquired from as-indicated treatment groups along with the representative mouse images. Scale bars are 200 μm for the H&E-stained images and 1 cm for the mouse images. (h) Hematological indexes and biochemical analyses of mouse blood, where the mice were intravenously injected with PBS and CMIR-CDa for 7 and 14 days, respectively. Statistical analysis was performed by two-tailed Student's t test (*p < 0.05, **p < 0.01, and ***p < 0.001).

After investigating the ROS generation properties, the *in vitro* cytotoxicity of CMIR-CDa was investigated by MTT (3-(4,5-dimethylthiazol-2-yl)-2,5-diphenyltetrazolium bromide) assay in 4T1 cells. Cell viability assessments revealed the cell viability of ~77.8% upon incubation with CMIR-CDa up to a concentration of 25 μg/mL without any external stimuli after 24 h (Figure S16). The high concentration of H_2O_2 in acidic TME allows the spontaneous Fenton-like reaction by CMIR-CDa inside cells and thereby should be accountable for the tumor cell death. The control study utilizing MIR-CDa indicated a low cell ablation ability through Fenton-like reaction without US irradiation, whereas IR-CDa displayed negligible cytotoxicity. Normal HEK293 cells still exhibited high viability upon the incubation with CMIR-CDa (up to 25 μg/mL) for 24 h (Figure S17). Interestingly, the efficacy of the Fenton or Fenton-like reaction was accelerated by the molecular turbulence created by US irradiation. When irradiated with US (1 W cm^{-2}) for 3 min, 25 μg/mL CMIR-CDa displayed an efficient cell ablation ability (the cell viability of ~28.3%) by a combination of ROS generation (Figure 4e). Compared to that of CMIR-CDa, the viability of 4T1 cells treated with MIR-CDa under US irradiation also noticeably decreased to about ~58.1%, exhibiting US-mediated ROS generation. In comparison, IR-CDa, capable of generating only $^1O_2$ under US irradiation, exhibited a cell viability of ~72.2%. The higher cell ablation efficacy by CMIR-CDa could be attributed to the enhanced ·OH and $O_2^{\bullet -}$ generation as compared to MIR-CDa, whereas their $^1O_2$ generation ability was inferred to be similar. Additionally, ROS cytotoxicity related cell death increased upon increasing the US power and US application time, further confirming the importance of using US as the external stimulus source (Figure S18).

To corroborate the results by CLSM, calcein AM and propidium iodide (PI) were utilized to stain the live and dead cells, respectively. In comparison with the control groups, CMIR-CDa with an efficient anticancer ability *via* US-enhanced ROS generation exhibited enhanced cytotoxicity under the US irradiation, as shown by prominent red fluorescence and very weak green fluorescence (Figure 4f). The control groups followed a similar trend to that of MTT assay, with IR-CDa possessing the least cell killing ability as compared to MIR-CDa and CMIR-CDa. Flow cytometry analysis supported the MTT results and live−dead cell assay, with CMIR-CDa showing US-enhanced ROS generation and tumor ablation (Figure 4g,h). A higher proportion of late apoptotic cells was assessed for US-enhanced CMIR-CDa group (66.7%), compared to 40.6% for US-enhanced MIR-CDa group.

https://doi.org/10.1021/jacsau.1c00422
JACS Au 2021, 1, 2328−2338

In Vivo Fluorescence Imaging and Photoacoustic Tomography

4T1-tumor-bearing BALB/c mice were utilized as a tumor xenograft model to investigate the tumor accumulation ability of CMIR-CDa *in vivo*. CMIR-CDa was administrated *via* intravenous injection, followed by the detection of fluorescence signal intensification in the tumor site overtime (Figure 5a). The results showed that CMIR-CDa accumulated at the tumor region, in accord with the EPR effect.[42,43] Fluorescence imaging studies at the tumor region indicated high nanoparticle accumulation at the tumor site at 12 h, with sustained fluorescence signals up to 24 h (Figure S19). *In vivo* fluorescence imaging using IR-CDa as a control exhibited similar tumor accumulation (Figure S20). To further detect the ideal therapeutic window for *in vivo* therapy, NIR-I photoacoustic tomography was performed on 4T1-tumor-bearing mice on a homemade photoacoustic system equipped with a 700 nm pulse laser.[44,45] CMIR-CDa exhibited a concentration-dependent linear increment of photoacoustic amplitude *in vivo* (Figure S21a). After systemic administration of CMIR-CDa, photoacoustic signals in the tumor region gradually increased and reached the maxima at 9 h post injection, suggesting the passive targeting of nanoparticles in the solid tumor due to their small hydrodynamic size and PEGylated surface (Figure S21b,c).

In Vivo Antitumor Efficacy

The *in vivo* antitumor efficiency of the CD assembly was evaluated using 4T1-tumor-bearing BALB/c mice. Prior to this study, the *in vivo* biodistribution of CMIR-CDa was explored (Figure S22). The tumor accumulation of Mo in 4T1-tumor-bearing mice reached a higher concentration as compared to that in other major organs after 24 h. For subsequent therapeutic experiments, 4T1 cells were subcutaneously inoculated in the right flank of mice (Figure 5b). After 7 days, the mice were segregated into five random groups: (I) control group (PBS), (II) CMIR-CDa, (III) IR-CDa + US, (IV) MIR-CDa + US, and (V) CMIR-CDa + US. After intravenous injection of respective assemblies, the tumor regions were treated with US as shown in the treatment schedule. The growth rate of the tumors was monitored every 2 days. In group II, the tumors were marginally shrunken in comparison to the control group I, indicating a therapeutic effect of TME-activated CDT through Fenton-like reaction. Upon US irradiation (1 W cm^{-2}, 3 min), groups III and IV showed a substantial reduction in tumor volume (Figure 5c). Additionally, group V exhibited substantial tumor growth repression as compared to other groups, reinforcing the antitumor efficiency through the enhanced ROS generation. Furthermore, all tumors were harvested after the treatments (Figure S23). The average weight of tumors from the CMIR-CDa group was only 0.112 g, much lower than other treatment groups (Figure 5d). The treatment groups showed no noticeable variation of body weights for all mice during 14-day monitoring (Figure 5e).

The therapeutic efficiency was additionally evaluated by histological examination. After the treatment with US-irradiated CMIR-CDa, the tumor tissues stained by hematoxylin and eosin (H&E) exhibited obvious dead cells in the images compared to the control groups, consistent with the observation of tumor volume reduction after the therapy (Figure 5f). The hemolysis test was conducted to examine the biocompatibility of CMIR-CDa in blood (Figure S24). No obvious hemolytic effect was observed in the assessed range. To assess the biosafety of CMIR-CDa-mediated therapy, blood biochemical study and histological analysis of the major organs were conducted. Blood biochemistry and hematological indexes were within normal range values, indicating no considerable side effect of CMIR-CDa over 7 and 14 day monitoring (Figure 5g).[46] Afterward, H&E staining images of the major organs (heart, liver, spleen, lung, kidney, and intestine) in treatment groups exhibited similar physiological morphologies compared to that in the control group, demonstrating a high biosafety of CMIR-CDa (Figure S25).

CONCLUSIONS

In summary, fluorescent CMIR-CDa was prepared from a mixture of IR-780, MoO_2Cl_2, and $Cu(acac)_2$, followed by cooperative self-assembly with DSPE-PEG to improve the biocompatibility and aqueous dispersity. The as-prepared CMIR-CDa could be utilized as a contrast agent for fluorescent imaging with high sensitivity. More importantly, CMIR-CDa could efficiently produce $O_2^{\bullet -}$ and $^1O_2$ upon low-density US irradiation. CMIR-CDa has been applied as the Fenton or Fenton-like catalyst to promote the generation of ·OH radical in TME, which could be further augmented by the US application. Detailed *in vitro* and *in vivo* studies have demonstrated that the as-prepared CMIR-CDa could be utilized as an ROS nanogenerator in the presence of US for fluorescent imaging-guided tumor ablation. The present work offers biomedical applications of hybrid CDs and provides a route toward carbon-based nanosystems for imaging-guided multimodal therapeutic applications.

EXPERIMENTAL METHODS

Synthesis of CMIR-CD

CMIR-CD was prepared by the solvothermal approach from $Cu(acac)_2$, MoO_2Cl_2, and IR-780 iodide. Briefly, $Cu(acac)_2$ (25 mg), MoO_2Cl_2 (25 mg), and IR-780 iodide (10 mg) were dispersed in absolute ethyl alcohol (50 mL) with ultrasonication for 30 min and then heated at 180 °C in an autoclave for a period of 24 h. After cooling to room temperature, CMIR-CD was obtained by removing larger nanoparticles using a 0.22 μm membrane filter and then free precursors through dialysis against ethyl alcohol several times.

Synthesis of CMIR-CDa

To improve the aqueous dispersity of CMIR-CD, DSPE-PEG (10 mg) in water (5 mL) was added dropwise into CMIR-CD ethanol solution (1 mL, 2.5 mg/mL). After 1 h of vigorous stirring at room temperature, CMIR-CDa was prepared by consequent dialysis (molecular weight cutoff: 3500 Da). IR-CDa (IR-780 CD assembly) and MIR-CDa (Mo and IR-780 CD assembly) were obtained as controls by following the same synthetic procedure as of CMIR-CDa, with necessary precursors.

Detection of Singlet Oxygen

Singlet oxygen sensor green (SOSG) reacts with $^1O_2$ to give rise to a bright green fluorescence (excitation/emission maxima 504/525 nm). CMIR-CDa, MIR-CDa, or IR-CDa was dispersed in water (2 mL, 25 μg/mL) in the presence of SOSG (12.5 μM). The mixed suspension was exposed to US (0.5 W cm^{-2}) for different periods, and the fluorescence was measured accordingly.

Detection of Superoxide

Dihydrorhodamine 123 (DHR 123) reacts with $O_2^{\bullet -}$ to give rise to a bright green fluorescence (excitation/emission maxima 505/529 nm). CMIR-CDa, MIR-CDa, or IR-CDa was dispersed in water (2 mL, 25 μg/mL) in the presence of DHR 123 (12.5 μM). The mixed

https://doi.org/10.1021/jacsau.1c00422
JACS Au 2021, 1, 2328−2338

suspension was exposed to US (0.5 W cm^{-2}) for different periods, and the fluorescence was measured accordingly.

Detection of Hydroxyl Radical

Terephthalic acid (TA) reacts with ·OH to give rise to a bright green fluorescence (excitation/emission maxima 326/432 nm). CMIR-CDa, MIR-CDa, or IR-CDa was dispersed in water (1 mL, 50 μg/mL) at pH 6.5 in the presence of TA (1 mL, 200 μg/mL). The mixed suspension was exposed to US (0.5 W cm^{-2}) for different periods, and the fluorescence was measured accordingly.

Cellular Uptake

CMIR-CDa (10 μg/mL), MIR-CDa (10 μg/mL), or IR-CDa (10 μg/mL) was incubated with the cultured 4T1 cells at 37 °C for 6 h. For a time-dependent uptake study, CMIR-CDa (10 μg/mL) was incubated with the cultured 4T1 cells at 37 °C for different periods (6, 3, and 1 h). The nuclei were stained by Hoechst 33342. After the incubation period, the cells were gently rinsed with PBS and examined by CLSM (Carl Zeiss LSM 800).

In Vitro Toxicity and Safety Study

The *in vitro* cytotoxicity was measured by following a standard MTT viability assay against 4T1 cells. Cells were seeded at a density of 5000 cells/well in 96-well plates and incubated overnight. Afterward, the cells were incubated with CMIR-CDa, MIR-CDa, and IR-CDa at different concentrations (0, 15, 20, and 25 μg/mL) at 37 °C in a 5% CO_2 atmosphere for 24 h, respectively. The formulation was changed with MTT-containing medium (5 mg/mL), and an additional 4 h incubation was conducted for the cells at a determined time. Then, MTT was removed and DMSO was dropped to dissolve the formazan crystals at 37 °C in the dark. A microplate reader (Tecan's Infinite M200 microplate reader) was used to measure the absorbance at 570 nm. Untreated cells represented 100% viability.

In Vitro Anticancer Therapy

Ninety-six-well plates were used to culture 4T1 cells at 37 °C for 24 h. CMIR-CDa, MIR-CDa, and IR-CDa at different concentrations (0, 10, 15, 20, and 25 μg/mL) were added and the treated cells were incubated in the dark, respectively. After 6 h, US (1 W cm^{-2}, 3 min) was applied on the treatment groups, which were further incubated for 24 h. Subsequently, a freshly prepared MTT working solution was added to each well and incubated at 37 °C for 4 h. After the reaction, the plate was measured on a microplate reader to read the absorbance at 570 nm. Cell viabilities were thus calculated as the ratio of the absorbance of cells with various treatments to that of the control cells without any treatments.

Live/Dead Staining

Six-well plates were used to culture 4T1 cells, which were incubated with CMIR-CDa, MIR-CDa, and IR-CDa (20 μg/mL), respectively. After 6 h of incubation, US (1 W cm^{-2}, 3 min) was applied on the treatment groups. Then, PI and calcein-AM were used to costain the treated cells. Lastly, the stained cells were examined by CLSM (Carl Zeiss LSM 800).

In Vivo Fluorescence Imaging

4T1-tumor-bearing BALB/c mice were treated with CMIR-CDa through intravenous injection for *in vivo* fluorescence imaging. Imaging was performed at different time points upon the injection under 676 nm excitation wavelength using an *in vivo* optical imaging system (IVIS spectrum-CT *In Vivo* Imaging System).

In Vivo Tumor Therapy

BALB/c mice bearing 4T1 tumors were randomly allocated into five groups (n = 5): (a) control, (b) CMIR-CDa, (c) IR-CDa + US, (d) MIR-CDa + US, and (e) CMIR-CDa + US. For US groups, after 24 h of intravenous injection of samples (50 μg/mL), the tumors of the mice were applied US (1 W cm^{-2}, 3 min). US was applied for three consecutive times (6, 24, and 48 h). Followed by the treatments, the sizes of tumors and the body weights of treated mice were measured every 2 days for 14 days. All the tumor volumes were computed according to the formula below:

$$\text{volume} = (\text{tumor length}) \times (\text{tumor width})^2/2\ (\text{mm}^3)$$

The relative tumor volume (V/V_0) was normalized to its initial size before the administration. After 14 days of different treatments, the mice in each treatment group were euthanized, and the tumor tissues and other organs were collected.

Histological Studies

After 14 days of different treatments, 4T1-tumor-bearing mice in each group were euthanized, and the tumors along with the major organs (heart, liver, spleen, lung, intestine, and kidney) were harvested and fixed with 4% paraformaldehyde for H&E staining. The stained tissue sections were assessed using a digital microscope.

■ ASSOCIATED CONTENT

Supporting Information

The Supporting Information is available free of charge at https://pubs.acs.org/doi/10.1021/jacsau.1c00422.

Discussions of reagents and materials used, measurements, intracellular ·OH, $^1O_2$, $O_2^{\bullet -}$, and total ROS detection assay, NIR-I photoacoustic tomography system, biochemical analysis of blood, and statistical analysis and figures of emission spectra, FTIR spectra, XPS analysis, TEM images, DLS curves, SOSG assay, terephthalic assay, CLSM images, relative fluorescence intensity, concentration-dependent cytotoxicity, ultrasound power-density- and time-dependent cytotoxicity, quantification of *in vivo* fluorescence images, NIR fluorescence images, linear fit of photoacoustic amplitudes, time-course NIR-I photoacoustic tomography, distribution of Mo in the major organs and tumor, photos of excised tumors from different treatment groups, hemolysis of CMIR-CDa at various concentrations, and H&E staining images (PDF)

■ AUTHOR INFORMATION

Corresponding Author

Yanli Zhao − *Division of Chemistry and Biological Chemistry, School of Physical and Mathematical Sciences, Nanyang Technological University, Singapore 637371, Singapore; School of Chemical and Biomedical Engineering, Nanyang Technological University, Singapore 637459, Singapore;* orcid.org/0000-0002-9231-8360; Email: zhaoyanli@ntu.edu.sg

Authors

Deblin Jana − *Division of Chemistry and Biological Chemistry, School of Physical and Mathematical Sciences, Nanyang Technological University, Singapore 637371, Singapore*

Dongdong Wang − *Division of Chemistry and Biological Chemistry, School of Physical and Mathematical Sciences, Nanyang Technological University, Singapore 637371, Singapore;* orcid.org/0000-0002-6278-0706

Praveenbalaji Rajendran − *School of Chemical and Biomedical Engineering, Nanyang Technological University, Singapore 637459, Singapore*

Anivind Kaur Bindra − *Division of Chemistry and Biological Chemistry, School of Physical and Mathematical Sciences, Nanyang Technological University, Singapore 637371, Singapore;* orcid.org/0000-0003-3722-0560

Yi Guo − *Division of Chemistry and Biological Chemistry, School of Physical and Mathematical Sciences, Nanyang Technological University, Singapore 637371, Singapore*

Jiawei Liu − *Division of Chemistry and Biological Chemistry, School of Physical and Mathematical Sciences, Nanyang Technological University, Singapore 637371, Singapore;* orcid.org/0000-0003-4011-3950

Manojit Pramanik − *School of Chemical and Biomedical Engineering, Nanyang Technological University, Singapore 637459, Singapore*

Complete contact information is available at: https://pubs.acs.org/10.1021/jacsau.1c00422

Author Contributions

The manuscript was written through contributions of all authors. All authors have given approval to the final version of the manuscript.

Notes

The authors declare no competing financial interest.

■ ACKNOWLEDGMENTS

This research was supported by the Singapore Agency for Science, Technology and Research (A*STAR) AME IRG grant (A20E5c0081) and the Singapore National Research Foundation Investigatorship (NRF-NRFI2018-03).

■ REFERENCES

(1) Gorrini, C.; Harris, I.; Mak, T. Modulation of Oxidative Stress as an Anticancer Strategy. *Nat. Rev. Drug Discovery* **2013**, *12*, 931−947.
(2) Trachootham, D.; Alexandre, J.; Huang, P. Targeting Cancer Cells by ROS-Mediated Mechanisms: A Radical Therapeutic Approach? *Nat. Rev. Drug Discovery* **2009**, *8*, 579−591.
(3) Yang, B.; Chen, Y.; Shi, J. Reactive Oxygen Species (ROS)-Based Nanomedicine. *Chem. Rev.* **2019**, *119*, 4881−4985.
(4) Ramsey, M. R.; Sharpless, N. E. ROS as a Tumour Suppressor? *Nat. Cell Biol.* **2006**, *8*, 1213−1215.
(5) Liu, C.; Cao, Y.; Cheng, Y.; Wang, D.; Xu, T.; Su, L.; Zhang, X.; Dong, H. An Open Source and Reduce Expenditure ROS Generation Strategy for Chemodynamic/Photodynamic Synergistic Therapy. *Nat. Commun.* **2020**, *11*, 1735.
(6) Luo, T.; Ni, K.; Culbert, A.; Lan, G.; Li, Z.; Jiang, X.; Kaufmann, M.; Lin, W. Nanoscale Metal-Organic Frameworks Stabilize Bacteriochlorins for Type I and Type II Photodynamic Therapy. *J. Am. Chem. Soc.* **2020**, *142*, 7334−7339.
(7) Silva, E. F.; Serpa, C.; Dabrowski, J. M.; Monteiro, C. J.; Formosinho, S. J.; Stochel, G.; Urbanska, K.; Simoes, S.; Pereira, M. M.; Arnaut, L. G. Mechanisms of Singlet-Oxygen and Superoxide-Ion Generation by Porphyrins and Bacteriochlorins and Their Implications in Photodynamic Therapy. *Chem. - Eur. J.* **2010**, *16*, 9273−9286.
(8) Dabrowski, J. M.; Arnaut, L. G.; Pereira, M. M.; Urbanska, K.; Simoes, S.; Stochel, G.; Cortes, L. Combined Effects of Singlet Oxygen and Hydroxyl Radical in Photodynamic Therapy with Photostable Bacteriochlorins: Evidence from Intracellular Fluorescence and Increased Photodynamic Efficacy *in Vitro*. *Free Radical Biol. Med.* **2012**, *52*, 1188−1200.
(9) Ranji-Burachaloo, H.; Gurr, P. A.; Dunstan, D. E.; Qiao, G. G. Cancer Treatment through Nanoparticle-Facilitated Fenton Reaction. *ACS Nano* **2018**, *12*, 11819−11837.
(10) Qian, X.; Zhang, J.; Gu, Z.; Chen, Y. Nanocatalysts-Augmented Fenton Chemical Reaction for Nanocatalytic Tumor Therapy. *Biomaterials* **2019**, *211*, 1−13.
(11) Wang, P.; Liang, C.; Zhu, J.; Yang, N.; Jiao, A.; Wang, W.; Song, X.; Dong, X. Manganese-Based Nanoplatform as Metal Ion-Enhanced ROS Generator for Combined Chemodynamic/Photodynamic Therapy. *ACS Appl. Mater. Interfaces* **2019**, *11*, 41140−41147.
(12) Liu, C.; Wang, D.; Zhang, S.; Cheng, Y.; Yang, F.; Xing, Y.; Xu, T.; Dong, H.; Zhang, X. Biodegradable Biomimic Copper/Manganese Silicate Nanospheres for Chemodynamic/Photodynamic Synergistic Therapy with Simultaneous Glutathione Depletion and Hypoxia Relief. *ACS Nano* **2019**, *13*, 4267−4277.
(13) Dong, S.; Xu, J.; Jia, T.; Xu, M.; Zhong, C.; Yang, G.; Li, J.; Yang, D.; He, F.; Gai, S.; Yang, P.; Lin, J. Upconversion-Mediated $ZnFe_2O_4$ Nanoplatform for NIR-Enhanced Chemodynamic and Photodynamic Therapy. *Chem. Sci.* **2019**, *10*, 4259−4271.
(14) Lei, Z.; Zhang, X.; Zheng, X.; Liu, S.; Xie, Z. Porphyrin-Ferrocene Conjugates for Photodynamic and Chemodynamic Therapy. *Org. Biomol. Chem.* **2018**, *16*, 8613−8619.
(15) Sengar, P.; Garcia-Tapia, K.; Chauhan, K.; Jain, A.; Juarez-Moreno, K.; Borbon-Nunez, H. A.; Tiznado, H.; Contreras, O. E.; Hirata, G. A. Dual-Photosensitizer Coupled Nanoscintillator Capable of Producing Type I and Type II ROS for Next Generation Photodynamic Therapy. *J. Colloid Interface Sci.* **2019**, *536*, 586−597.
(16) Pillar-Little, T. J.; Wanninayake, N.; Nease, L.; Heidary, D. K.; Glazer, E. C.; Kim, D. Y. Superior Photodynamic Effect of Carbon Quantum Dots through Both Type I and Type II Pathways: Detailed Comparison Study of Top-Down-Synthesized and Bottom-Up-Synthesized Carbon Quantum Dots. *Carbon* **2018**, *140*, 616−623.
(17) Wang, W.; Zhang, Q.; Zhang, M.; Liu, Y.; Shen, J.; Zhou, N.; Lu, X.; Zhao, C. Multifunctional Red Carbon Dots: A Theranostic Platform for Magnetic Resonance Imaging and Fluorescence Imaging-Guided Chemodynamic Therapy. *Analyst* **2020**, *145*, 3592−3597.
(18) Riley, P. R.; Narayan, R. J. Recent Advances in Carbon Nanomaterials for Biomedical Applications: A Review. *Curr. Opin. Biomed. Eng.* **2021**, *17*, 100262.
(19) Arcudi, F.; Đorđević, L.; Prato, M. Design, Synthesis, and Functionalization Strategies of Tailored Carbon Nanodots. *Acc. Chem. Res.* **2019**, *52*, 2070−2079.
(20) Jia, Q.; Ge, J.; Liu, W.; Zheng, X.; Chen, S.; Wen, Y.; Zhang, H.; Wang, P. A Magnetofluorescent Carbon Dot Assembly as an Acidic H_2O_2-Driven Oxygenerator to Regulate Tumor Hypoxia for Simultaneous Bimodal Imaging and Enhanced Photodynamic Therapy. *Adv. Mater.* **2018**, *30*, 1706090.
(21) Wen, Y.; Jia, Q.; Nan, F.; Zheng, X.; Liu, W.; Wu, J.; Ren, H.; Ge, J.; Wang, P. Pheophytin Derived Near-Infrared-Light Responsive Carbon Dot Assembly as a New Phototheranotic Agent for Bioimaging and Photodynamic Therapy. *Chem. - Asian J.* **2019**, *14*, 2162−2168.
(22) Canavese, G.; Ancona, A.; Racca, L.; Canta, M.; Dumontel, B.; Barbaresco, F.; Limongi, T.; Cauda, V. Nanoparticle-Assisted Ultrasound: A Special Focus on Sonodynamic Therapy against Cancer. *Chem. Eng. J.* **2018**, *340*, 155−172.
(23) de Leon, A.; Perera, R.; Nittayacharn, P.; Cooley, M.; Jung, O.; Exner, A. A. Ultrasound Contrast Agents and Delivery Systems in Cancer Detection and Therapy. *Adv. Cancer Res.* **2018**, *139*, 57−84.
(24) Shibaguchi, H.; Tsuru, H.; Kuroki, M.; Kuroki, M. Sonodynamic Cancer Therapy: A Non-Invasive and Repeatable Approach Using Low-Intensity Ultrasound with a Sonosensitizer. *Anticancer Res.* **2011**, *31*, 2425−2429.
(25) Gong, F.; Cheng, L.; Yang, N.; Gong, Y.; Ni, Y.; Bai, S.; Wang, X.; Chen, M.; Chen, Q.; Liu, Z. Preparation of $TiH_{1.924}$ Nanodots by Liquid-Phase Exfoliation for Enhanced Sonodynamic Cancer Therapy. *Nat. Commun.* **2020**, *11*, 3712.
(26) Han, X.; Huang, J.; Jing, X.; Yang, D.; Lin, H.; Wang, Z.; Li, P.; Chen, Y. Oxygen-Deficient Black Titania for Synergistic/Enhanced Sonodynamic and Photoinduced Cancer Therapy at Near Infrared-II Biowindow. *ACS Nano* **2018**, *12*, 4545−4555.
(27) Son, S.; Kim, J. H.; Wang, X.; Zhang, C.; Yoon, S. A.; Shin, J.; Sharma, A.; Lee, M. H.; Cheng, L.; Wu, J.; Kim, J. S. Multifunctional Sonosensitizers in Sonodynamic Cancer Therapy. *Chem. Soc. Rev.* **2020**, *49*, 3244−3261.
(28) Li, Y.; Zhou, Q.; Deng, Z.; Pan, M.; Liu, X.; Wu, J.; Yan, F.; Zheng, H. IR-780 Dye as a Sonosensitizer for Sonodynamic Therapy of Breast Tumor. *Sci. Rep.* **2016**, *6*, 25968.
(29) Chang, N.; Qin, D.; Wu, P.; Xu, S.; Wang, S.; Wan, M. IR780 Loaded Perfluorohexane Nanodroplets for Efficient Sonodynamic

Effect Induced by Short-Pulsed Focused Ultrasound. *Ultrason. Sonochem.* **2019**, *53*, 59−67.
(30) Zhang, L.; Yi, H.; Song, J.; Huang, J.; Yang, K.; Tan, B.; Wang, D.; Yang, N.; Wang, Z.; Li, X. Mitochondria-Targeted and Ultrasound-Activated Nanodroplets for Enhanced Deep-Penetration Sonodynamic Cancer Therapy. *ACS Appl. Mater. Interfaces* **2019**, *11*, 9355−9366.
(31) Ma, B.; Wang, S.; Liu, F.; Zhang, S.; Duan, J.; Li, Z.; Kong, Y.; Sang, Y.; Liu, H.; Bu, W.; Li, L. Self-Assembled Copper-Amino Acid Nanoparticles for in Situ Glutathione "AND" H_2O_2 Sequentially Triggered Chemodynamic Therapy. *J. Am. Chem. Soc.* **2019**, *141*, 849−857.
(32) Lin, L. S.; Huang, T.; Song, J.; Ou, X. Y.; Wang, Z.; Deng, H.; Tian, R.; Liu, Y.; Wang, J. F.; Liu, Y.; Yu, G.; Zhou, Z.; Wang, S.; Niu, G.; Yang, H. H.; Chen, X. Synthesis of Copper Peroxide Nanodots for H_2O_2 Self-Supplying Chemodynamic Therapy. *J. Am. Chem. Soc.* **2019**, *141*, 9937−9945.
(33) Wang, D.; Wu, H.; Wang, C.; Gu, L.; Chen, H.; Jana, D.; Feng, L.; Liu, J.; Wang, X.; Xu, P.; Guo, Z.; Chen, Q.; Zhao, Y. Self-Assembled Single-Site Nanozyme for Tumor-Specific Amplified Cascade Enzymatic Therapy. *Angew. Chem., Int. Ed.* **2021**, *60*, 3001−3007.
(34) Tang, Z.; Liu, Y.; He, M.; Bu, W. Chemodynamic Therapy: Tumour Microenvironment-Mediated Fenton and Fenton-like Reactions. *Angew. Chem., Int. Ed.* **2019**, *58*, 946−956.
(35) Liu, G.; Zhu, J.; Guo, H.; Sun, A.; Chen, P.; Xi, L.; Huang, W.; Song, X.; Dong, X. Mo_2C-Derived Polyoxometalate for NIR-II Photoacoustic Imaging-Guided Chemodynamic/Photothermal Synergistic Therapy. *Angew. Chem., Int. Ed.* **2019**, *58*, 18641−18646.
(36) Chen, Q.; Yang, D.; Yu, L.; Jing, X.; Chen, Y. Catalytic Chemistry of Iron-Free Fenton Nanocatalysts for Versatile Radical Nanotherapeutics. *Mater. Horiz.* **2020**, *7*, 317−337.
(37) Hu, X.; Li, F.; Xia, F.; Guo, X.; Wang, N.; Liang, L.; Yang, B.; Fan, K.; Yan, X.; Ling, D. Biodegradation-Mediated Enzymatic Activity-Tunable Molybdenum Oxide Nanourchins for Tumor-Specific Cascade Catalytic Therapy. *J. Am. Chem. Soc.* **2020**, *142*, 1636−1644.
(38) Chang, M.; Wang, M.; Wang, M.; Shu, M.; Ding, B.; Li, C.; Pang, M.; Cui, S.; Hou, Z.; Lin, J. A Multifunctional Cascade Bioreactor Based on Hollow-Structured Cu_2MoS_4 for Synergetic Cancer Chemo-Dynamic Therapy/Starvation Therapy/Phototherapy/Immunotherapy with Remarkably Enhanced Efficacy. *Adv. Mater.* **2019**, *31*, 1905271.
(39) Sun, S.; Chen, Q.; Tang, Z.; Liu, C.; Li, Z.; Wu, A.; Lin, H. Tumor Microenvironment Stimuli-Responsive Fluorescence Imaging and Synergistic Cancer Therapy by Carbon-Dot−Cu^{2+} Nanoassemblies. *Angew. Chem.* **2020**, *132*, 21227−21234.
(40) Jana, D.; Wang, D.; Bindra, A. K.; Guo, Y.; Liu, J.; Zhao, Y. Ultrasmall Alloy Nanozyme for Ultrasound- and Near-Infrared Light-Promoted Tumor Ablation. *ACS Nano* **2021**, *15*, 7774−7782.
(41) Wang, D.; Jana, D.; Zhao, Y. Metal-Organic Framework Derived Nanozymes in Biomedicine. *Acc. Chem. Res.* **2020**, *53*, 1389−1400.
(42) Fang, J.; Nakamura, H.; Maeda, H. The EPR Effect: Unique Features of Tumor Blood Vessels for Drug Delivery, Factors Involved, and Limitations and Augmentation of the Effect. *Adv. Drug Delivery Rev.* **2011**, *63*, 136−151.
(43) Jana, D.; Jia, S.; Bindra, A. K.; Xing, P.; Ding, D.; Zhao, Y. Clearable Black Phosphorus Nanoconjugate for Targeted Cancer Phototheranostics. *ACS Appl. Mater. Interfaces* **2020**, *12*, 18342−18351.
(44) Rajendran, P.; Sahu, S.; Dienzo, R. A.; Pramanik, M. *In Vivo* Detection of Venous Sinus Distension Due to Intracranial Hypotension in Small Animal Using Pulsed-Laser-Diode Photoacoustic Tomography. *J. Biophotonics* **2020**, *13*, e201960162.
(45) Das, D.; Sharma, A.; Rajendran, P.; Pramanik, M. Another Decade of Photoacoustic Imaging. *Phys. Med. Biol.* **2021**, *66*, 05TR01.
(46) Wang, D.; Wu, H.; Yang, G.; Qian, C.; Gu, L.; Wang, H.; Zhou, W.; Liu, J.; Wu, Y.; Zhang, X.; Guo, Z.; Chen, H.; Jana, D.; Zhao, Y. Metal−Organic Framework Derived Multicomponent Nanoagent as a Reactive Oxygen Species Amplifier for Enhanced Photodynamic Therapy. *ACS Nano* **2020**, *14*, 13500−13511.

https://doi.org/10.1021/jacsau.1c00422
JACS Au 2021, 1, 2328−2338